

# Highly Adaptive and Automated Tetrahedral Mesh Generator for Multi-Compartment Human Head Model with Deep Brain Structures in EEG

Fernando Galaz Prieto<sup>1\*</sup>, Joonas Lahtinen<sup>1</sup>, Yusuf Oluwatoki Yusuf<sup>1</sup>, Atena Rezaei<sup>1</sup> and Sampsa Pursiainen<sup>1</sup>

<sup>1\*</sup>Computing Sciences, Faculty of Information Technology and Communication Sciences, Korkeakoulunkatu 3, Tampere, 33014, Pirkanmaa, Finland.

\*Corresponding author(s). E-mail(s): [fernando.galazprieto@tuni.fi](mailto:fernando.galazprieto@tuni.fi);

## Abstract

**Background and Objective:** This paper introduces a highly adaptive and automated approach for generating Finite Element (FE) discretization for a given realistic multi-compartment human head model obtained through magnetic resonance imaging (MRI) dataset. We aim at obtaining accurate tetrahedral FE meshes for electroencephalographic source localization. **Methods:** We present recursive solid angle labeling for the surface segmentation of the model and then adapt it with a set of smoothing, inflation, and optimization routines to further enhance the quality of the FE mesh. **Results:** The results show that our methodology can produce FE mesh with an accuracy greater than 1 millimeter, significant with respect to both their 3D structure discretization outcome and electroencephalographic source localization estimates. **Conclusions:** FE meshes can be achieved for the human head including complex deep brain structures. Our algorithm has been implemented using the open Matlab-based Zeffiro Interface toolbox with its effective time-effective parallel computing system.

**Keywords:** Mesh Generation, Finite Element Method (FEM), Inverse Problem, Boundary Conditions, Electroencephalography (EEG)

## 1 Introduction

This paper introduces a highly adaptive approach for generating a volumetric Finite Element (FE) mesh [1–3] for a realistic multi-compartment human head model obtained from magnetic resonance imaging (MRI) data. Such mesh is required for performing accurate simulation of electromagnetic fields and propagation. A solution to the Maxwell’s electromagnetic field equations given a

source of the field can be considered as a forward mapping for various inverse modelling and imaging applications. We consider, in particular, non-invasive Electroencephalography (EEG) [4] wherein the activity of the brain is observed by measuring the electric potential field via a set of contact electrodes attached on skin. EEG inverse problems are ill-posed [5], that is, their solutions are non-unique, are sensitive to noise and modelling errors, and strongly rely on the accuracy

of the solution for the EEG forward problem [6–8], where electric potentials need to be simulated using a realistic head volume conductor model. The sub-cortical components are known to be especially sensitive and distinguishable with non-invasive data as it has been recently shown in [9–11].

The Finite Element Method (FEM) [3] is an advantageous method for modelling the head and its electromagnetic fields since it enables both surface- and volumetric-based mesh adaptation. FE mesh generation for the human head poses a challenging mathematical modelling task as the head includes various internal layers with their own complex and geometrical properties. Well-known heuristic FE mesh generators such as TetGen [12], Netgen [13] and Gmsh [14] principally aim at reconstructing non-intersecting surfaces and, consequently, might not be applicable for a complex brain geometry in their standard form. Thus, to obtain high-quality FE mesh, a tailored solution devoted to the brain and head structure is needed. Earlier solutions for optimized FE mesh generation include, for example, SimBio-Vgrid<sup>1</sup> which has been extensively applied in FEM-based EEG studies [15, 16], and coupling the TetGen mesh generator with other tools such as the implementation in Matlab’s iso2mesh toolbox [17]. With this study, we aim to provide an effective and automated alternative to perform a complete FE meshing process for an arbitrary number of cortical and sub-cortical compartments without the need of mesh pre-processing or combining different tools, such as in the recent study [18]. To accomplish this task, our approach incorporates advanced features such as FE meshing of a complete head segmentation found by FreeSurfer Software Suite [19], robustness with respect to intersecting surfaces, and a time-effective Graphic Processing Unit (GPU) accelerated recursive labeling process.

In this paper, we describe a method to obtain an optimized FE mesh with accuracy greater than 1 millimeter (mm), which is shown to be a crucial aspect from the physical and physiological viewpoint [2]. Our method is divided in the (I) mesh generation and (II) post-processing stage. In the first stage (I), we describe the generation of regular mesh, refinement of tetrahedra, and application of the recursive solid angle labeling process

for a multi-compartment surface segmentation [20]; as a result, this allows the mesh to match a set of closed segmentation boundaries in which the tissue structure can be either (a) complex-shaped (e.g., cerebral cortex and sub-cortical nuclei), (b) thin-layered (skin), or (c) include material properties whose electrical conductivity can include a steep contrast (skin–skull–cerebrospinal fluid (CSF) boundaries) [21]. The second stage (II) consist of the surface smoothing, inflation, and optimization steps. The labeling process is shown to be the predominating factor in determining the computational cost of mesh generation and effectively parallelizable either in a central or graphics processing unit (CPU or GPU).

We measure the accuracy of the EEG lead field matrices obtained with adaptive vs. regular meshes, and perform a series of EEG source localization experiments to assess the quality of these mesh. For model reference, we used a spherical three-layered Ary model and a Magnetic Resonance Imaging (MRI) based multi-compartment realistic head model [22] obtained using the FreeSurfer. For source localization [23], we used the minimum norm estimate (MNE) [24], standardized low-resolution brain electromagnetic tomography (sLORETA) [25], and dipole scan, also known as the deviation scan [26] (the simplest form of beamformer). For result corroboration, we examine 14 and 22 ms median nerve stimulus responses reconstructed from experimental Somatosensory Evoked Potential (SEP) data [22, 27] using a combination of sLORETA and Gaussian Mixture Modelling (GMM) [28].

Our results show that a robust FE mesh can be produced and the adaptive approach is significant considering the 3D structure of the outcome of the discretization, and the source localization estimates of EEG. Our algorithm has been implemented using the open Matlab-based Zeffiro Interface forward and inverse toolbox<sup>2</sup>, [27, 29, 30], whose forward solver has previously been built upon a high-resolution regular meshing approach. This study shows that mesh adaptation provides a significant improvement in accuracy without leading to significantly greater computing times, credited to recursive re-labeling and GPU acceleration.

---

<sup>1</sup><http://vgrid.simbio.de>

<sup>2</sup>[https://github.com/sampsapursiainen/zeffiro\\_interface](https://github.com/sampsapursiainen/zeffiro_interface)

## 2 Methodology

### 2.1 Mesh generation

To obtain an appropriate FE mesh [20] for an arbitrary surface-based head tissue segmentation, we implement a hierarchical approach for filling the complete computation domain  $\Omega$  where the tissue compartments are assumed to be nested. Each of the layers corresponding to the mesh presented are labeled from the innermost to the outermost one. The boundary that comes first in the layer hierarchy will be prioritized whenever there is an occurrence of intersecting segmentation boundaries. The number of compartments included in the model can be arbitrary, thus a bounding box is used as the outermost compartment which is removed after the mesh creation has been finalized. This will prevent any optimization based shrinkage effects that otherwise might take place on the external surface.

#### 2.1.1 Regular meshing

The meshing process begins by setting a regular hexahedral lattice in the domain. Each hexahedra is then subdivided into five (5) tetrahedra elements (See Figure 1) which is the lowest possible number of tetrahedral subdivisions [31]. This is an advantageous way to convert a hexahedral lattice into a tetrahedra leading to an alternating direction of the diagonal subdividing the edges over the adjacent hexahedra. As a result, this transformation restricts the generation of weighted directional bias which affects mesh manipulation operations, i.e., smoothing and inflation procedures. Moreover, this also minimizes the amount of total memory required to support the dataset.

#### 2.1.2 Mesh refinement

The mesh can be refined with respect to either a given sub-domain  $V$  or to its boundary  $\partial V$  (see Figure 2). The elements in  $V$  are subdivided into eight (8) tetrahedra faces, while in  $\Omega \setminus V$ —those having nodes adjacent to the boundary  $\partial V$ —are subdivided to their corresponding number of edges shared with  $\partial V$ .

#### 2.1.3 Labeling

To obtain the compartment of a given element, we use solid angle labeling method [20]. That is,

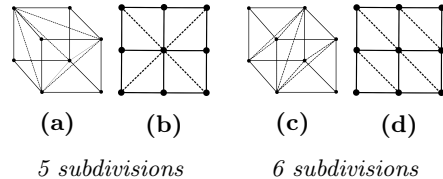


**Fig. 1.** A schematic illustration of an (1a) hexahedra subdivided into five tetrahedra [31]. We have chosen this subdivision strategy as we consider the resulting (planar) alternating pattern of faces and edges in adjacent hexahedra (1b) advantageous to reduce any potential lattice-dependent effects in the final processed mesh. In contrast, a subdivision into six (6) tetrahedra (1c) results into a non-alternating pattern creating potential geometrical bias, e.g., directional bias of smoothing (1d).

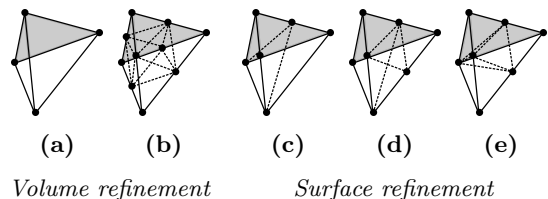


**Fig. 2.** A schematic illustration of the volume and surface refinement. In volume refinement, each tetrahedral element (2a) in a given subdomain  $S$  of  $\Omega$  is subdivided into eight tetrahedra (2b). The refined volume  $S$  is connected to the remaining part of the domain  $\Omega \setminus S$  via surface refinement layer where the elements can have one to three edges subdivided on the face adjacent to the boundary  $\partial S$ , leading to tetrahedral subdivisions (2c, 2d, 2e), respectively. A refinement with respect to a boundary  $\partial S$  can be defined as two similar refinements on both sides of  $\partial S$ .

a mesh node at position  $\vec{r}_i$  is associated with the integral

$$s_i = \frac{1}{4\pi} \int_{\partial S} (\vec{r} - \vec{r}_i) \cdot \vec{n} dA, \quad (1)$$

where  $\partial S$  is a closed segmentation boundary,  $dA$  is a surface area differential, and  $\vec{n}$  is the normal vector at the point  $\vec{r}$ . The integral  $s_i$  can be interpreted as the ratio between the full solid angle and the angle covered by  $\partial S$  with respect to the point  $\vec{r}_i$ . It is interpreted that  $\vec{r}_i$  is enclosed by  $\partial S$  if

$s_i >= T$  with  $T$  denoting a given threshold value between 0 and 1. Those tetrahedra that have four nodes inside  $\partial S$  are labeled as the elements contained by  $S$ . The tetrahedral mesh boundary  $\partial V$  of the labeled compartment  $V$  approximates  $\delta S$ . Labeling can be applied in the following two ways:

1. Initial labeling: all nodes within a tetrahedral mesh are labeled using the solid angle method.
2. Recursive re-labeling (see figure 3): the tissue boundaries in an already existing mesh are re-labeled after changing their nodes, e.g., due to refinement. That is, for each labeling-based tissue boundary, the solid angle integral  $s$  is re-evaluated for the nodes shared by the tetrahedra adjacent to the boundary. Thus, the labels of the tetrahedra are updated potentially changing the tissue boundary. The process will be repeated recursively until convergence, i.e., when the status of one or more nodes remains unchanged.

Once the regular mesh has been generated, initially labeled, refined and then re-labeled, the resulting tetrahedral mesh can be post-processed via smoothing inflation and optimization steps to fit any tetrahedral compartment surface  $\partial V$  included in the mesh with the corresponding segmentation boundary  $\partial S$ .

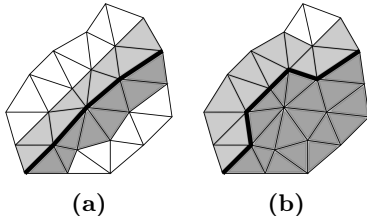


**Fig. 3.** Recursive solid angle labeling process re-labels the tetrahedra (here presented by triangles) adjacent to a given boundary  $\partial V$  (black curve) between two different tissue compartments (light and dark grey). The re-labeling process is performed until  $\partial V$  does not change between two consecutive recursion steps, as it does between (3a) and (3b).

### 2.1.4 Computational considerations

The recursive re-labeling provides a way to reduce computation cost since, instead of the full

3D set of nodes, it processes 2D boundary-based sets which have considerably less entries due to their lower dimensional extent. Therefore, the resolution of the segmentation boundary  $\partial S$  is an important factor regarding the cost. To avoid an excessive cost while maintaining accuracy on an appropriate level, we consider setting the density or mesh size of  $\partial S$  to be approximately that of the tetrahedral mesh.

## 2.2 Post processing

### 2.2.1 Smoothing

As a smoothing technique, we use the Taubin's method [32], which performs Laplacian forward and backward smoothing steps alternating to smooth the mesh and to reduce shrinkage, respectively. Both volume and tissue boundaries are smoothed using the following formula:

$$\vec{x}_i^{(k+1/2)} = \vec{x}_i^{(k)} + \lambda \sum_{j \in \mathcal{N}_i} x_j^k, \quad (2)$$

$$\vec{x}_i^{(k+1/2)} = \vec{x}_i^{(k)} - \mu \sum_{j \in \mathcal{N}_i} x_j^{(k+1/2)}, \quad (3)$$

where  $\lambda < 1$  and  $\mu < 1$  are smoothing parameters and the index set  $\mathcal{N}_i$  contains  $\vec{x}_i^{(k)}$  together with its neighbors. In surface smoothing,  $\mathcal{N}_i$  includes those node indices belonging to a given surface boundary sharing an edge with  $\vec{x}_i^{(k)}$ . In volumetric smoothing, all the neighbors connected by an edge with  $\vec{x}_i^{(k)}$  are included in  $\mathcal{N}_i$ . The stopping criterion for smoothing is set to be

$$\frac{\|\vec{x}^{(k+1/2)} - \vec{x}^{(k)}\|_2}{\|\vec{x}^{(0)}\|_2} \leq \xi, \quad (4)$$

where  $\xi$  is a user-defined value.

### 2.2.2 Inflation

After performing labeling and re-labeling routines, the surface  $\partial V$  is then enclosed by the segmentation boundary  $\partial S$  as each tetrahedra adjacent to  $\partial V$  has now its four nodes inside  $\partial S$ . Once four nodes had been enclosed, they are then lifted by inflation. This method is accomplished by initially detecting the intersecting edges in  $\partial S$ , followed by determining the intersection point, and finally sliding the nodes of  $\partial V$  towards those points along

their associated edges. The amount of inflation for a given intersecting edge is calculated via the formula:

$$\vec{x}_i^{(1)} = \vec{x}_i^{(0)} + \zeta d\vec{e}, \quad (5)$$

where  $\vec{e}$  is a unit vector parallel to the edge,  $d$  is the distance between  $\vec{x}_i$  and  $\partial S$ , and  $\zeta < 1$  is an inflation parameter.

### 2.2.3 Optimization

After smoothing and inflation, the optimization step finalizes the post-processing in two phases ensuring that the elements generated are valid and have an appropriate condition which we measure by the volume  $\mathcal{V}_T$  of a given tetrahedron divided by the length of its longest edge  $\ell_T^{(\max)}$ , i.e.,

$$\kappa = \frac{\mathcal{V}_T}{\ell_T^{(\max)}}. \quad (6)$$

Here  $\kappa$  is called the condition number. In the first phase, the optimization process searches for inverted tetrahedras, i.e., elements with a negative determinant. The inverted elements are fixed by bringing any node  $\vec{x}$  that is outside the outer surface of its associated supernode, i.e., the set containing all the neighbors sharing an edge with  $\vec{x}$ , back inside this surface. This process is repeated recursively until there are no inverted elements. The second phase performs Delaunay turns [3, 33] for each pair of adjacent elements in which the condition number is smaller than a given threshold  $\tau$ , ( $\kappa < \tau$ ), at least, in one of the two tetrahedras. Of the two different possible orientations of the shared face, the one for which the minimal condition number is larger is selected.

## 2.3 EEG modelling

We tested the performance of the present mesh generation routine in numerical EEG modelling. In EEG, an unknown primary source current distribution  $\vec{\mathbf{J}}_{\mathbf{p}}$  generated by the brain activity is to be localized in the brain given a set of point measurements  $\mathbf{y}$  of the electric potential distribution  $\mathbf{u}$ . Given  $\vec{\mathbf{J}}_p$ , the electric potential can be obtained as a solution of the second-order partial differential equation

$$\nabla \cdot (\sigma \nabla u) = \nabla \cdot \vec{\mathbf{J}}_p, \quad (7)$$

which holds under the quasi-static approximation where  $\sigma$  is the electric conductivity distribution affecting the solution significantly.

Equation (7) can be expressed in a discretized form  $\mathbf{Az} = \mathbf{Gx}$ , where the vectors  $\mathbf{z}$  and  $\mathbf{x}$  discretize the volumetric distributions of  $u$  and  $\vec{\mathbf{J}}_p$ , and the matrices  $\mathbf{A}$  and  $\mathbf{G}$  the operators acting on both left- and right-side, respectively. Solving the discretized form with respect to  $\mathbf{z}$  and taking into account that  $\mathbf{y}$  can be obtained by multiplying  $\mathbf{z}$  with a restriction matrix  $\mathbf{R}$ , i.e.,  $\mathbf{y} = \mathbf{Rz}$ , implies the linear forward model

$$\mathbf{y} = \mathbf{Lx}, \quad (8)$$

where  $\mathbf{L} = \mathbf{RA}^{-1}\mathbf{G}$  is the so-called lead field matrix.

Equation (8) poses an ill-posed inverse problem with respect to the unknown activity  $\mathbf{x}$ . That is, the solution is non-unique and even a slight amount of noise in the measurement data can have a significant effect on a candidate solution. The source currents corresponding to the entries of  $\mathbf{x}$  are assumed to be dipolar [34].

To obtain the lead field matrix, we apply the FEM together with the divergence conforming H(div) source model [7] allowing to approximate dipolar sources. The position based optimization (PBO) technique [7, 35] was applied to obtain the source orientations and positions. To solve the inverse problem, we apply the following three alternative well-known source localization methods described below.

### 2.3.1 Minimum norm estimation

Minimum Norm Estimate (MNE) [24] is evaluated as the solution of the following Tikhonov regularized maximization problem:

$$\min_{\mathbf{x}} \left\{ \|\mathbf{Lx} - \mathbf{y}\|^2 + \|\lambda \mathbf{Cx}\|^2 \right\}, \quad (9)$$

where  $\mathbf{C}$  is the noise covariance matrix and  $\lambda$  is the penalty term. This problem can be associated with a Bayesian setting in which both the prior and likelihood have Gaussian densities [27]. The regularization parameter can be interpreted as a prior-over-measurement signal-to-noise ratio (PM-SNR), i.e., the relative weight of the prior compared to the likelihood.

### 2.3.2 Standardized low-resolution brain electromagnetic tomography

Standardized low-resolution brain electromagnetic tomography (sLORETA) is a re-weighted MNE reconstruction, where the weighting coefficients are inversely proportional to noise variances reconstructed via MNE (9). Consequently, the energy of the reconstruction is not affected by the variable amplitude of the lead field in different parts of the domain where the reconstruction is found [25].

### 2.3.3 Dipole scan

Dipole scan [26] refers to evaluating the following goodness of fit (GOF)  $g$  between the data and a dipole at the  $i$ -th position of the source space:

$$g = 1 - \frac{\|\mathbf{y} - \mathbf{L}_i \mathbf{L}_i^\dagger \mathbf{y}\|^2}{\|\mathbf{y}\|^2} \quad (10)$$

Here  $\mathbf{L}_i$  is the submatrix of  $\mathbf{L}$  which contains the source or sources associated with the  $i$ -th position. The reconstruction is a distribution of GOFs covering the whole source space.

### 2.3.4 Analytical solution

On a spherical domain, the numerical ground truth can be obtained via the analytical solution of a dipolar electric potential field which, in a homogeneous medium, is of the form

$$u_j^{(h)} = \frac{1}{4\pi\epsilon_0\epsilon_r} \frac{\vec{q} \cdot \vec{r}}{\|\vec{r}\|^2}, \quad (11)$$

for a dipole with a moment  $\vec{q}$  placed at the point  $\vec{r}$ , with  $\epsilon_0$  denoting the electric permittivity of the vacuum and  $\epsilon_r$  the relative permittivity of the medium. For a multi-layer sphere, consisting of multiple concentric spherical compartments, the field can be approximated through the sum  $u_j(\vec{q}, \vec{r}) \approx \sum_{\ell=1}^K u_j^{(h)}(\lambda_\ell \vec{q}, \mu_\ell \vec{r})$ , where  $\lambda_\ell$  and  $\mu_\ell$  are so-called Berg parameters that can be obtained via numerical optimization [36, 37].

### 2.3.5 Earth mover's distance

To measure the accuracy of a source localization estimate with respect to a given dipole, we use the earth mover's distance (EMD) which measures the minimum amount of work required to transfer a given mass distribution to another one. The

measure was first proposed as an analytical distance function between probability distributions in metric spaces in [38, 39]. The linear optimization task and the name of EMD originate from [40]. In this study, we use EMD to measure the similarity between a distributional reconstruction and a dipole associated with Dirac's delta function (or unit impulse).

### 2.3.6 Gaussian mixture modeling

For the realistic head model, we analyze the source localization estimates via clustering as there is no ground truth for such a case. As a clustering technique, we use Gaussian Mixture Modelling (GMM) [28], where an estimate of the primary current density is assumed to be given and the task is to find its main concentration areas as a mixture, i.e., a superposition of Gaussian distributions. We assume that the current density estimate forms a single or multi-modal distribution of source activity, where an individual mean location of a distribution component gives the most probable location of the corresponding neural activity. By assigning the weight

$$w_i = \frac{\|\vec{J}(\vec{r}_i)\|_2^2}{\sum_{j=1}^N \|\vec{J}(\vec{r}_j)\|_2^2}^{-1}, \quad (12)$$

for a given reconstruction  $\vec{J}$  and each source point  $\vec{r}_i$ ,  $i = 1, 2, \dots, N$ , GMM can detect a controlled number of neural activity clusters contained by  $\vec{J}$ . The clusters are added in the cluster configuration recursively via a deterministic process of selecting the best fitting set with respect to a probability-thresholded Mahalanobis distance [41] not yet added into the configuration. Moreover, the most fitting number of Gaussian components can be decided through the GMM algorithm by selecting the model with the lowest Bayes Information Criterion (BIC).

## 3 Numerical experiments

This section describes the numerical experiments performed with the present adaptive FEM mesh generation routine. Both the spherical three-layer Ary model and the realistic head model were utilized as a computational domain. The EEG forward simulation and source localization accuracy

were analyzed in both cases. Four initial mesh resolutions were used; an adaptive mesh was created beginning from a hexahedral lattice size of 3.0, 2.0 and 1.3 mm, and a regular mesh was obtained by subdividing a lattice with 1.0 mm edge-length into tetrahedra.

### 3.1 Spherical three-layer Ary model

The three-layer Ary model [42] is composed of three concentric spheres with radii 87, 92 and 100 mm and conductivities 0.33, 0.0042 and 0.33 S/m (Siemens per meter), respectively. The steep contrast between the adjacent brain and skull layers poses a challenge for the forward simulation and dipole localization which have been analyzed using a universal heuristic mesh generator in [43]. The Berg parameters of the analytical solution can be found therewithin. The present numerical experiments were performed referring to 180 point electrodes evenly spread over the external surface.

### 3.2 Realistic head segmentation

The realistic head model was obtained from an openly available dataset<sup>3</sup> [22] including MRI data of a healthy 48 years old adult subject. To segment the data, the standard reconstruction procedure of the FreeSurfer Software Suite<sup>4</sup> was applied, resulting in 18 volumetric compartments altogether. The segmentation of the subcortical regions corresponded to FreeSurfer's Aseg Atlas. The tissue conductivities were selected according to their literature reference values [21] for scalp (0.33 S/m), skull (0.0064 S/m), CSF (1.79 S/m), gray matter (0.33 S/m), and white matter (0.14 S/m). For the subcortical compartments, the value 0.33 S/m was chosen [44].

### 3.3 Finite element meshes

To avoid redundant computing in the labeling phase the FE mesh generation process begins by first evaluating the density of the surface segmentation. If the calculated density is greater than the initial FE mesh resolution, it downsamples the segmentation to match with resolution of said FE mesh; the tissue boundaries of the volumetric mesh are then refined once for the active

compartments, including both the cerebral and cerebellar cortex as well as the deep active nuclei. The smoothing parameters are set to be equal  $\lambda = \mu = 0.4$  while the stopping criterion was  $\xi = 0.9$  for the volumetric smoothing and  $\xi = 0.1$  for surface smoothing. The inflation parameter was chosen to be  $\zeta = 0.05$ .

#### 3.3.1 Source space

Each EEG lead field matrix was generated using the divergence conforming [7] source model for a set of 10,000 source positions, uniformly distributed over the domain  $\Omega$ . In the spherical Ary model, a source triplet corresponding to the three Cartesian orientations was associated with each source position. In the realistic head model, the sources were otherwise composed of Cartesian triplets but normally constrained with respect to the compartment surface in the cerebral and cerebellar cortices and hippocampi, following the orientation of the neurons and neural activity in these compartments [45].

### 3.4 Somatosensory evoked potential data

The package [22] includes a 74-channel EEG measurement dataset from a somatosensory evoked potential (SEP) experiment, where the median nerve of the right wrist was stimulated via monophasic square-wave electrical pulses with 0.5 millisecond duration. The SEPs revealed by these measurements have been investigated in [27], suggesting that the originators of both sub-cortical and cortical early responses can be approximately localized using non-invasive data. In this study, we approximate the originators of the P14/N14 and P22/N22 (14 and 22 millisecond post-stimulus, respectively) peaks using via sLORETA/GMM reconstructions and lead field matrices obtained with different FE meshes. The first one of these peaks is originated in the medial lemniscus of the brain stem above the cuneate nucleus [46–50], while the second one is originated in two locations: a cortical originator has been observed in the crown of either the first pre- or post-central gyrus [26, 51, 52], and a sub-cortical one in thalamus [53].

---

<sup>3</sup><https://doi.org/10.5281/zenodo.3888381>

<sup>4</sup><https://surfer.nmr.mgh.harvard.edu/>

### 3.5 Analysis of FE mesh quality

The accuracy of each mesh was evaluated by measuring the distance between the surface of the grey matter compartment and the actual tissue boundary of the segmentation. The element condition distribution was evaluated for each mesh. In addition, an overall analysis of the meshing outcome was performed visually.

For the spherical model, the lead field matrix accuracy was evaluated at different eccentricities values, i.e., relative distances from the origin in the brain compartment using the relative difference (RDM) and magnitude (MAG) measures [7]:

$$\text{RDM}(\vec{j}_1, \vec{j}_2) = \left\| \frac{\vec{j}_1}{\|\vec{j}_1\|_2} - \frac{\vec{j}_2}{\|\vec{j}_2\|_2} \right\|_2 \quad (13)$$

$$\text{MAG}(\vec{j}_1, \vec{j}_2) = 1 - \left( \frac{\|\vec{j}_1\|_2}{\|\vec{j}_2\|_2} \right). \quad (14)$$

Here,  $\vec{j}_1$  and  $\vec{j}_2$  denote FEM-based and analytical forward models, respectively. The analytical sources have random orientations but share the same set of positions with their FEM-based approximations. The RDM reflects the topographical forward modeling error in terms of location and orientation while MAG reflects the variations in potential amplitude; distributional source localization estimates were calculated for 4 different sets of 18 dipoles placed at eccentricities 0.06, 0.29, 0.63 and 0.98, evaluating the EMD between the actual dipole source and the estimate.

### 3.6 Computing platform

The numerical results were computed using a Dell Precision 5820 Workstation with 256 GigaByte (GB) Random Access Memory (RAM), 10-core Intel i9-10900X Central Processing Unit (CPU), and NVidia Quadro RTX 4000 Graphics Processing Unit (GPU). As two alternative solutions for parallelizing the labeling process, both CPU and GPU were applied. In the CPU parallelization, ten serial execution threads were run simultaneously (one per CPU core), whereas in GPU the process was decomposed into individually handled blocks of ten vectorized labeling operations.

## 4 Results

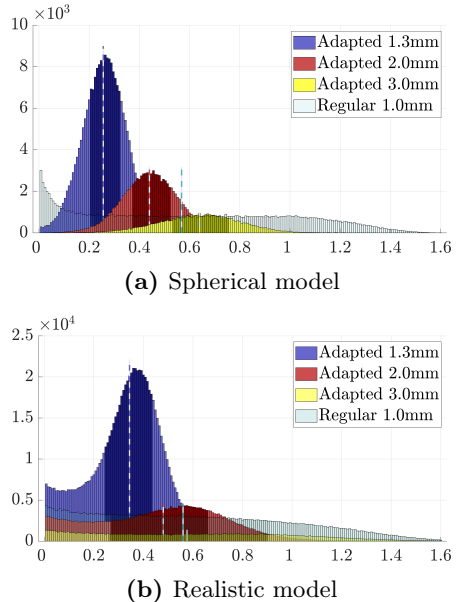


**Fig. 4.** Histograms for the spherical three-layer Ary model (4a) and realistic head model (4b) depicting the distance between the grey matter boundary in the FE mesh and in the segmentation.

The downsampled surface segmentation (triangular) and volumetric (tetrahedral) FE mesh parameters for each model are presented in Table 1. The computing times (measured in seconds) for each case have been included in Table 2 and 3. The finest overall FE mesh was obtained with 1.3 mm initial lattice resolution which resulted in 5.0, 7.5 million (M) nodes and 27, 40 M tetrahedra for the spherical and realistic model, respectively.

The results suggest that the recursive re-labeling method applied in adaptive mesh generation allows faster meshing with respect to the mesh size as compared to the regular approach. Overall, a major computing effort is spent on labeling, which can be accelerated when performed in GPU. This is clearly shown by the computing times obtained; GPU labeling took, in many cases less than 1/10 the time consumed by CPU. The effect of the labeling was the most significant in the case of regular mesh, where the recursive surface extraction (Section 2.1.3) was not applied. In adaptive meshing, the GPU accelerated total

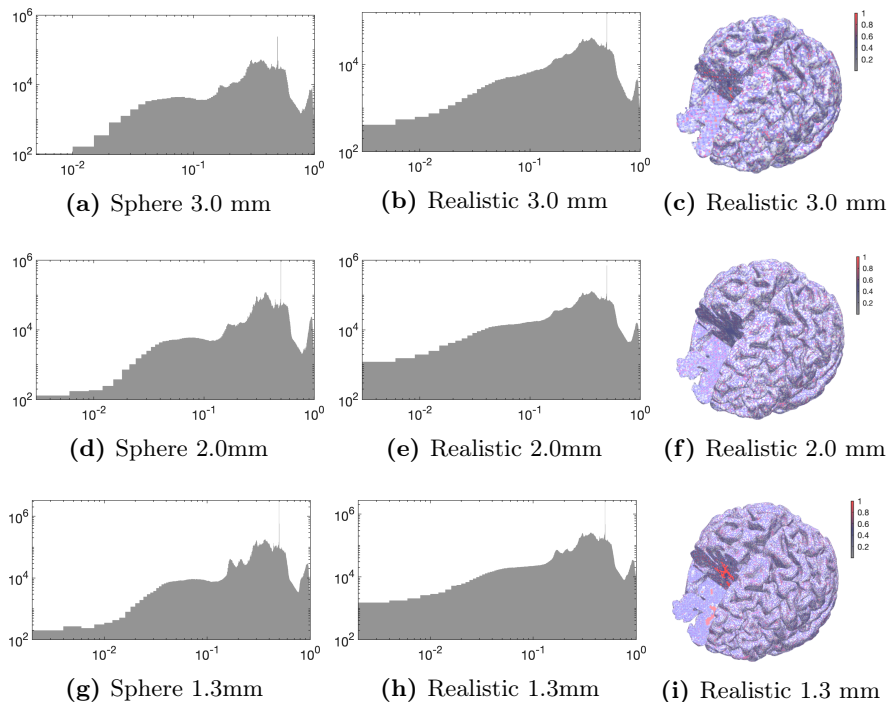


**Fig. 5.** Element condition distributions of the adapted 3.0, 2.0 and 1.3 mm FE mesh shown as a histogram for the spherical three-layer Ary model (5a, 5d, 5g) and realistic head model (5b, 5e, 5h). The spatial condition number mappings (5c, 5f, 5i) for the realistic head model show as expected that the non-refined internal parts of the mesh, in particular, the interior of the white matter, correspond to an elevated condition compared to the thin refined layers closer to the surface.

meshing time was close to 1/3–1/2 compared to the case of no acceleration. The post-processing phase, i.e., smoothing, inflation and optimization, took roughly 30-40 % of the total required time by the GPU accelerated meshing, being the larger the mesh, the less significant one.

The distance between the given and the reconstructed grey matter boundary is shown in Figures (4a) and (4a). In the spherical case, the median of this distance is close to one fourth of the initial mesh resolution, i.e., one half of the refined mesh size in the vicinity of the boundary. For the realistic case, the errors were slightly larger and more disperse, the median and spread (inter-quartile range between the 25 and 75 % quantiles) being smaller than the refined mesh size. The regular mesh can be observed to have a comparably large spread following from the absence of the smoothing and inflation steps.

The element condition distributions are shown in Figure 5. The distributions obtained for the

spherical and realistic mesh can be observed to be mainly similar. The proportion of the elements with condition below 0.01 is, however, considerably emphasized for the realistic meshes as compared to the spherical ones, which can be understood as a consequence of greater number of smoothed surfaces. The spatial condition number mappings for the realistic head model show as expected that the non-refined internal parts of the mesh, in particular, the interior of the white matter, correspond to an elevated condition compared to the thin refined layers closer to the surface.

The effect of the mesh adaptation is illustrated in Figure 6 and 7 for the spherical and realistic cases, respectively. The effect of surface refinement is clearly visible in the case of adapted 1.3 mm mesh; the resolution of an adapted FE mesh decreases towards the interior in the compartments that share the refined boundaries, while the in the regular mesh it is the same everywhere.

**Table 1:** The number of points and triangles for (downsampled) surface segmentations together with the node and tetra count for the FE meshes obtained using the spherical three-layer Ary model and a realistic head model.

Property	3.0mm	Adapted 2.0mm	1.3mm	Regular 1.0mm
Points	34,773	42,284	42,284	42,284
Triangles	72,556	88,636	88,636	88,636
Nodes	607,184	1,833,945	5,003,931	4,269,175
Tetras	3,245,733	9,903,208	26,801,840	20,871,950
Size (MB)	707	1,860	5,092	6,612

(a) Spherical overview.

Property	3.0mm	Adapted 2.0mm	1.3mm	Regular 1.0mm
Points	46,555	104,684	186,057	186,057
Triangles	93,016	209,314	372,088	372,088
Nodes	837,029	2,517,262	7,526,427	4,798,880
Tetras	4,540,361	13,699,905	40,895,474	23,460,830
Size (MB)	1,297	2,812	7,254	6,463

(b) Head model overview.

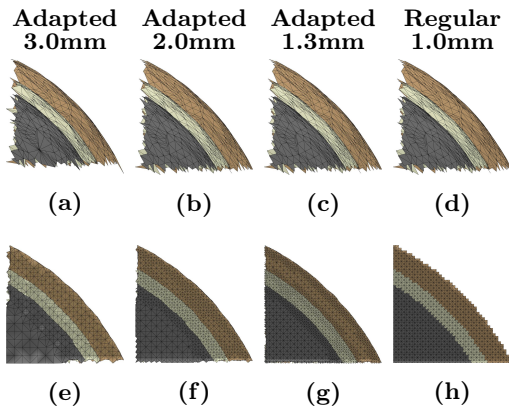


**Fig. 6.** Quadrants of the adapted surface- (6a-6c) and volume- (6e-6g) based reconstructions of the spherical three-layer Ary model depicting proposed mesh generation and post-processing methods using 3.0, 2.0 and 1.3 millimeter mesh sizes, respectively. Regular surface- (6d) and volume- (6h) with 1.0 mm mesh size without post-processing effect are included for comparison. The presented layers are (top-bot): scalp (brown), skull (white) and gray matter.

In Figure 8 we show reconstructions of the cerebrum, cerebellum and brain stem, and in Figure 9 the deep brain components including hippocampus, amygdala, putamen, thalamus caudate, ventricles, and cingulate cortex, both from

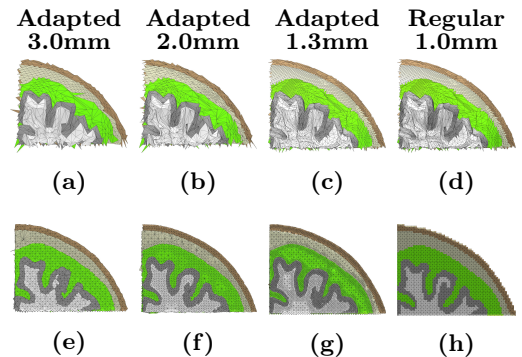


**Fig. 7.** Quadrants of the adapted surface- (7a-7c) and volume- (7e-7g) based reconstructions of the realistic head model depicting proposed mesh generation and post-processing methods using 3.0, 2.0 and 1.3 millimeter mesh sizes, respectively. Regular surface- (7d) and volume- (7h) with 1.0 mm mesh size without post-processing effect are included for comparison. The presented layers (top-bot) are: scalp (dark brown), skull (light brown), cerebrospinal fluid (green), gray matter, and white matter.

the same volumetric MRI data set described from 3.2. An increase in the mesh resolution can be observed to improve the shape and structure of the modelled tissues, which is particularly prominent for the caudal anterior area of the cingulate cortex which is not fully reconstructed in the case of the

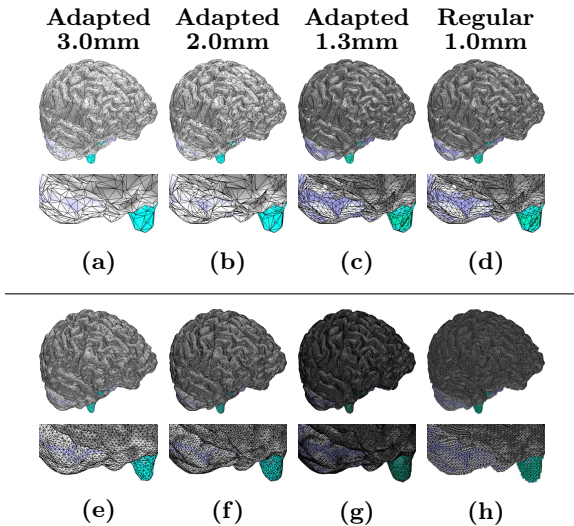


**Fig. 8.** Reconstruction of a realistic head model depicting the performance of adaptive FE mesh generation using 3.0, 2.0 and 1.3 mm mesh sizes (Surface: (8a-8c); Volume: (8e-8g), respectively) after applying recursive solid angle labeling, smoothing, inflation and optimization procedures in contrast with a regular 1.0 mm mesh generation without post-process procedures (8d and 8h). Regular mesh with 1.0 mm mesh size without post-processing effect is included for comparison. Cerebrum (gray), cerebellum (light blue) and brain stem (cyan).

3.0 mm resolution, obviously due to a comparably coarse initial resolution.

#### 4.1 EEG forward modelling

The RDM and MAG obtained with the spherical geometry are visualized in Figure 10. The adaptive meshes resulted in systematically more accurate lead field matrices. The smallest differences were obtained in the adapted 1.3 mm case. For each lead field matrix, the RDM had median below 5 % and MAG below 20 % up to 0.95. For the adapted meshes, these medians did not exceed 3 and 5 %. With the finest adapted mesh, the upper limits 3 and 4 % were maintained for eccentricities up to 0.998. The effect of adapting was pronounced towards the high eccentricities as is shown by the growing spread of the RDM and MAG distributions.

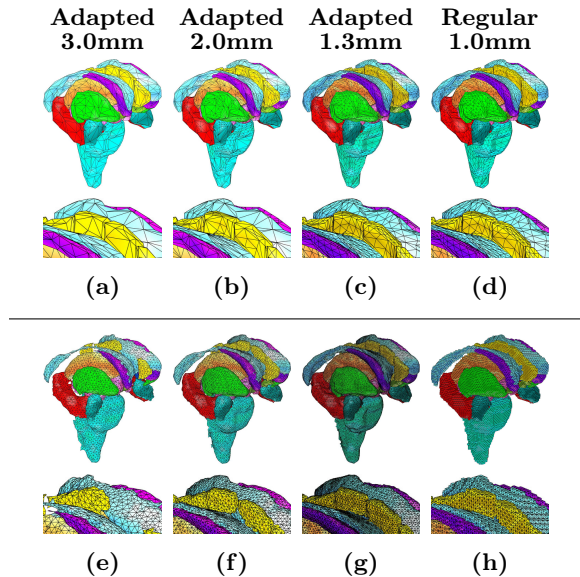
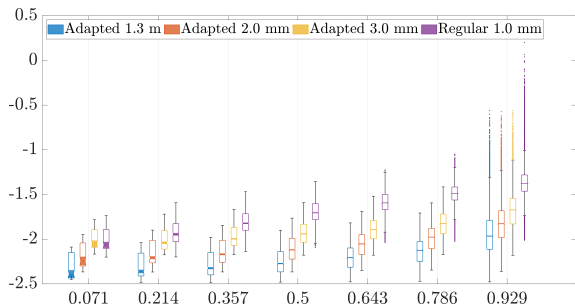


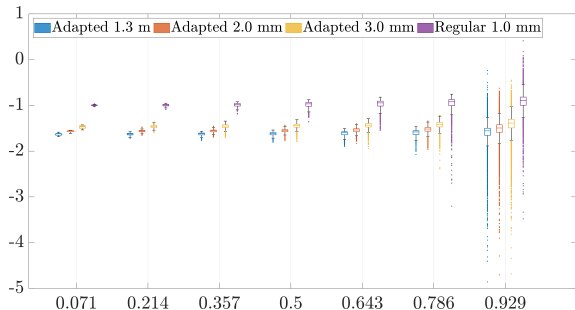
**Fig. 9.** Reconstruction of the deep structures for a realistic head model featuring the brain stem (cyan), hippocampus (red), amygdala (dark green), putamen (light green), thalamus (orange), caudate (purple), ventricles (blue), and cingulate cortex (yellow) depicting the performance of adaptive FE mesh generation using 3.0 mm, 2.0 mm and 1.3 mm mesh sizes (Surface: 9a-9c; Volume: 9e-9g, respectively) after applying recursive solid angle labeling, smoothing, inflation and optimization procedures in contrast to a regular 1.0 mm mesh generation without post-process procedures (9d and 9h). The focused image beneath illustrates that with a coarser mesh size over a complex domain the solver can yield inaccurate results, e.g., an incomplete cingulate cortex, while using a finer mesh size, e.g., 2.0 mm or lower, can model it with accuracy.

#### 4.2 Source localization

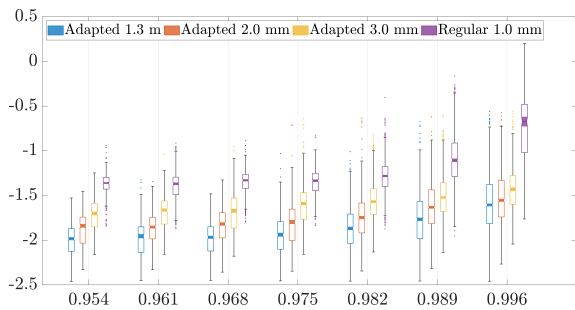
The source localization estimates for the spherical geometry and four different eccentricities, 0.06, 0.29, 0.63, and 0.98 %, are shown in Figure (11). The relative mutual differences between the adaptive and regular meshing approach, measured via EMD, were observed to be less prominent in source localization as compared to forward modelling. These EMD differences also depend on the applied inverse method. Matching with the forward simulation results, the adaptive 1.3 mm mesh provided the smallest median in each case



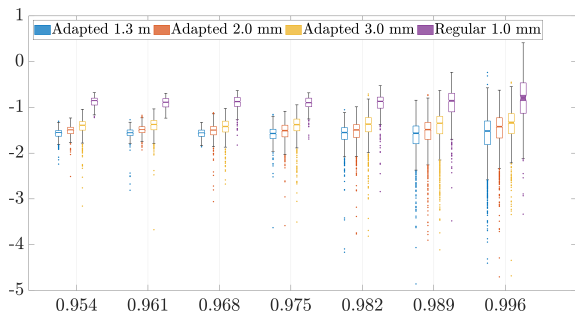
(a) Full-range Relative Difference (RDM)



(b) Full-range Magnitude (MAG)

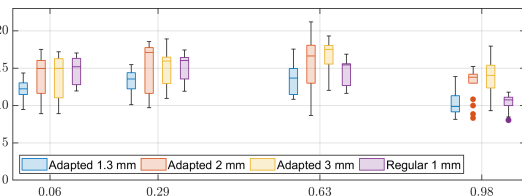


(c) 95% - 99% Relative Difference (RDM)

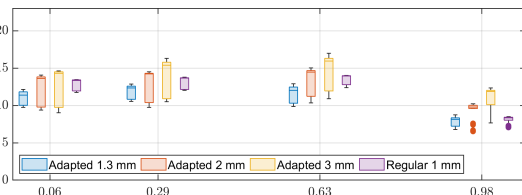


(d) 95% - 95% Magnitude (MAG)

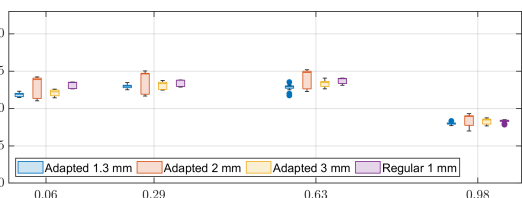
**Fig. 10.** Accuracy of the spherical three-layer Ary model in EEG forward modelling evaluated at different eccentricities levels, i.e., relative distances from the origin in the brain compartment using Relative Difference (RDM) and Magnitude (MAG).



(a) MNE



(b) sLORETA



(c) Dipole scan

**Fig. 11.** The earth mover's distance (EMD) measuring the amount of work required to transfer a distributional reconstruction into a dipole distribution (Dirac's delta) using Minimum Norm Estimation (MNE) (11a), Standardized low-resolution brain electromagnetic tomography (sLORETA) (11b), and Dipole scan (11c).

with a maximally 3.0 mm marginal to the other cases. For MNE and sLORETA, the initial FE mesh resolution (3.0, 2.0 and 1.3 mm) seems the governing factor determining the differences in source localization accuracy, while for Dipole scan such a tendency was not observed with the mutual differences between the methods being minor. In each case, the EMDs grow towards the centre of the domain (median 8–14 mm in the vicinity of the boundary and 12–15 mm near the centre) which is a natural consequence of the ill-posed nature of the source localization problem.

### 4.3 SEP components P14/N22 and P22/N22

The GMM clusters found corresponding to the SEP components P14/N22 and P22/N22 are

shown in Figure 12. The cluster volumes and their best fitting cluster counts can be found in Table 4. The clusters have been color-labeled according to their intensities (R=red, G=green, B=blue) in descending order.

For P14/N14, a single cluster concentrated at the brain stem was found in the case of the adapted 1.3 mm mesh, which is in accordance with the physiological knowledge of the originator, see Section 3.4. Two clusters were found with adapted 2 and 3 mm meshes, while the regular one resulted in three reconstructed clouds which is somewhat contrary to the knowledge of a single originator. The weaker clouds were larger in size, suggesting that they are due to modelling errors, as the actual originator is known to be well-localized in the brain stem.

For P22/N22, three clouds were obtained with each FE mesh. The distinction of the two most intense clouds R and G into a cortical and thalamic component was the clearest with 1.3 mm mesh. With the other meshes the clusters were closer to each other or they overlapped; in particular, the centroid of the most intense cluster was located deeper in the brain, suggesting that the reconstructed cortical and sub-cortical activity were partially mixed in the distribution found by sLORETA. The weaker clusters were larger in size, suggesting that they corresponded to modelling errors.

## 5 Discussion

This study has demonstrated an openly available [29] Matlab code which independently creates a FE mesh [1, 3] automatically for a multi-compartment model of the human head including both cortical and sub-cortical compartments. The realistic meshes generated on this study was shown to match the given complete head segmentation obtained using FreeSurfer Software Suite [19].

Our approach is based on nested compartment structures allowing a robust mesh generation for an arbitrary set of segmentation boundaries. One of the benefits that our method presents is the capability to generate a mesh regardless of intersecting segmentation boundaries inhibiting the issues that can follow from intersecting surfaces when using a standard heuristic FE mesh generator [12–14]. The resolution of the FE mesh

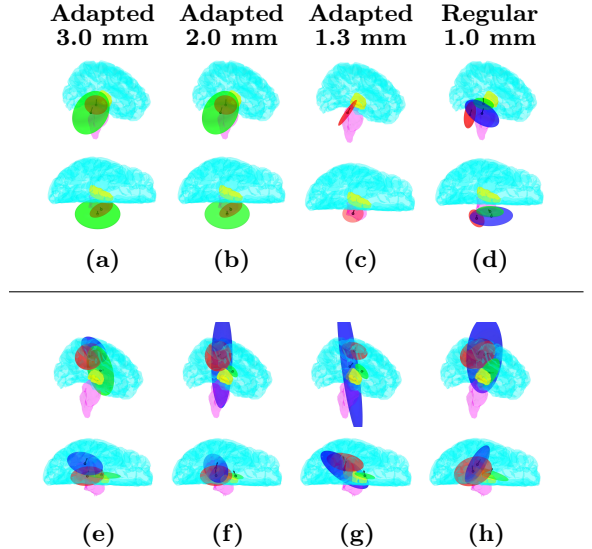


**Fig. 12.** Gaussian Mixture Modelling (GMM) clusters obtained for the P14/N14 (12a–12d) and P22/N22 (12e–12h) components of the experimental SEP dataset [22, 27]. Each cloud visualized shows the 90 % credibility set of the corresponding cluster. The clouds are color-labeled according to their measured intensities levels in cubic/millimeter ( $\text{mm}^3$ ).

was shown to be adaptable in the vicinity of the tissue boundaries, which was found to be essential to allow reducing the forward modelling and source localization errors that are likely to occur in those areas. The recursive labeling approach was found to save computational cost for both generating the mesh itself and obtaining high-quality FE simulation results with the segmentation. GPU-accelerated recursive labeling was shown to further speed up the mesh generation process as compared to a CPU-only implementation.

The meshing results were analyzed for three different initial hexahedral lattice resolutions, from coarse to fine, 3.0, 2.0, 1.3 mm. Due to adaptation, each meshes surpassed the 1 mm accuracy considering the distance spread between the given and reconstructed grey matter boundary. The regular 1 mm mesh had the largest spread which was clearly reflected in the measures for EEG modelling accuracy. Previously, a mesh size of about 1 mm or finer has been shown to be crucial for obtaining a rigorous EEG forward model e.g. in [2]. Because the computing effort increases greatly

**Table 2:** Total computation time (seconds) in CPU (top) and GPU parallelized (bottom) FE mesh creation of the spherical three-layer Ary model including post-processing methods, and Matlab’s data handling.

Function	Adapted			Regular
	3.0mm	2.0mm	1.3mm	1.0mm
Surface extraction	65	177	746	910
Labeling	318	1002	3308	6860
Refinement	9	25	73	0
Smoothing	61	161	443	0
Inflation	49	124	352	0
Optimization	30	92	413	0
Data handling	20	95	148	148
<b>Total</b>	552	1676	5483	7918
Surface extraction	62	206	646	896
Labeling	32	72	178	248
Refinement	9	24	70	0
Smoothing	59	150	417	0
Inflation	48	118	323	0
Optimization	28	88	365	0
Data handling	18	49	140	144
<b>Total</b>	256	707	2139	1288

**Table 3:** Total computation time (seconds) in CPU (top) and GPU parallelized (bottom) FE mesh creation of the realistic head model including post-processing methods, and Matlab’s data handling.

Function	Adapted			Regular
	3.0mm	2.0mm	1.3mm	1.0mm
Surface extraction	593	2329	7473	4800
Labeling	965	4508	24466	55574
Refinement	12	46	250	0
Smoothing	58	187	518	0
Inflation	290	856	2375	0
Optimization	146	398	856	0
Data handling	27	76	205	197
<b>Total</b>	2091	8400	36143	60571
Surface extraction	550	2292	7625	4447
Labeling	162	390	1410	2048
Refinement	11	44	252	0
Smoothing	55	165	516	0
Inflation	278	759	2260	0
Optimization	135	402	920	0
Data handling	20	76	200	150
<b>Total</b>	1212	4128	13183	6654

along with the initial mesh resolutions, the cases of 3.0 and 2.0 mm can be considered suitable to be used without GPU acceleration, e.g., with a laptop, while a higher resolution should be considered otherwise. In particular, the small sub-cortical details, such as the structure of the cingulate cortex, were found to necessitate the finest adapted mesh resolution in order to be labeled correctly.

The finest adapted mesh was found to outperform the regular 1 mm mesh in both EEG

forward simulation and source localization. With the finest adapted mesh, the median forward accuracy obtained at 98 % corresponded to 1.1 % RDM and 2.8 % MAG. For comparison, in [7, 30] approximately 0.3 % RDM and 0.3 % MAG were obtained with an optimized spherical Stok model [54] using a mesh created with Gmsh. The current results can be considered to be in an appropriate agreement with these, as Ary model [42] has been

**Table 4:** Volume-value of the up-to-three obtained GMM-based clusters (R=Red, G=Green, B=Blue) ordered in descending order with respect to their intensity, and measured in cubic millimeters ( $\text{mm}^3$ ).

<b>P14/N14 component</b>			
<b>Mesh size</b>	<b>R</b>	<b>G</b>	<b>B</b>
Adapted 3.0 mm	889	34104	-
Adapted 2.0 mm	889	34104	-
Adapted 1.3 mm	455	-	-
Regular 1.0 mm	393	333	6537

(a) Volume of the P14/N14 clusters.

<b>P22/N22 component</b>			
<b>Mesh size</b>	<b>cR</b>	<b>cG</b>	<b>cB</b>
Adapted 3.0 mm	2612	4581	5697
Adapted 2.0 mm	2606	10	22317
Adapted 1.3 mm	2353	23	46303
Regular 1.0 mm	9915	824	31988

(b) Volume of P22/N22 clusters.

observed to yield up to three times the errors obtained with Stok [43], following from the direct contact between the brain and skull compartment, which in Stok have a CSF layer inbetween them. Direct comparison between different meshing approaches is also not fully justified; the current strategy sets comparably soft requirements for the surface accuracy to avoid consequences of overfitting in the realistic case which might be reflected in the results.

In source localization, the median EMD found with the finest adapted mesh, 8–10 mm for the superior locations and 12–13 for the deeper ones with 2 mm spread in each case, matches well the experimentally found estimates for the best possible source localization accuracy in a spherical geometry which is 9.2 and 12.8 mm with a standard deviation of 4.4 and 6.2 mm, respectively [10]. The adapted 2 and 3 mm meshes were found to be computationally lighter, especially considering systems without GPU, while providing an appropriate modelling accuracy considering practical applications; the forward accuracy was found to be superior to that of the regular 1 mm mesh, while in source localization they were slightly less robust and lacked some accuracy with MNE and sLORETA, the deterioration being of maximally 4 mm considering median values. This lack falls

in the standard deviation suggested for the experimental case [10] and can be interpreted as a lattice or interpolation effect [7, 35], where sources that are further apart from each other than in a denser mesh are used in interpolating a given source. Namely, the differences observed are close to the initial mesh resolution in size.

The GMM clusters, including count, position and size, obtained using the experimental SEP data [22] suggest that the resolution of the mesh can have a significant effect on the inverse estimates obtained with a realistic setting considering all mesh resolutions examined in this study. Reflecting the physiological knowledge to number, size and positioning of the GMM clusters found [26, 46–53], a high resolution and mesh adaptation seem potentially beneficial ways to improve the reconstructions of P14/N14 and P22/N22 components. This observation concerned especially the adapted 1.3 mm case and is in line with the other results of this study. Obviously, due to its sensitivity to modelling errors, the deep activity of P14 component was found to deviate between the lead fields obtained with different meshes. The sensitivity of P22/N22 not only follows from its deep contribution but also from the simultaneous cortical originator in the pre- or post-central gyrus. The GMM deviations induced by the different FE meshes highlight the importance of accurate forward modelling and that even a few percent differences in RDM and/or MAG can lead to significant effects, when reconstructing weakly distinguishable activity. Previously, the detectability of the P14/N22 and P22/N22 originators has been suggested and analyzed in [27]. The distinguishability of the deep sub-cortical components based on non-invasive experimental EEG data has been suggested only recently [9].

Compared to SimBio-Vgrid driven studies [15, 16], we utilized a higher number of compartments including a complete set of sub-cortical compartments. Whereas our present approach constitutes an independent and time-effective tetrahedral mesh generator, which does not necessitate additional pre-processing, advanced tetrahedral meshes for the brain have been created recently by coupling multiple pre-processing tools with the well-known mesh generators, perhaps most prominently, Matlab’s toolbox iso2mesh [17]. In [55], iso2mesh-based mesh generator has been introduced for transcranial electrical stimulation. In

[18], a tetrahedral discretization of FreeSurfer’s Aseg atlas has been obtained using a combination of Computational Geometry Algorithms Library (CGAL) [56] and iso2mesh, resulting in a FE mesh of 0.8 M nodes and 5.3 M tetrahedra. In the light of our current results, a finer mesh might be necessary to completely distinguish the deeper structures as they appear in the Aseg atlas, justifying the examination of denser meshes and GPU acceleration as a way to speed up the labeling process.

Our future work will include further tests with experimental data as well as methodological and computational considerations, e.g., possibilities to speed up the surface extraction process, which is a major contributor to the total meshing time and involves complex indexing operations. The present meshing approach will be applied in the further development of advanced FEM forward simulation tools such as Duneuro [57] or packages for analyzing the brain activity, e.g., the current implementation platform ZI [29]. It can potentially provide future directions to develop similar platforms such as the well-known Brainstorm [58] whose forward model has been originally built upon the boundary element method.

**Acknowledgments.** *Funding.* FGP, JL, YOY, AR, and SP were supported by the Academy of Finland Centre of Excellence in Inverse Modelling and Imaging 2018–2025 and ERA PerMed Project (AoF, 344712) "Personalised diagnosis and treatment for refractory focal paediatric and adult epilepsy" (PerEpi). JL is supported by Väisälä Fund’s (Finnish Academy of Science and Letters) one-year young researcher grant admitted in 2021. *Conflicts of interest.* The authors certify that this study is a result of purely academic, open, and independent research. They have no affiliations with or involvement in any organization or entity with financial interest, or non-financial interest such as personal or professional relationships, affiliations, knowledge or beliefs, in the subject matter or materials discussed in this manuscript.

## References

- [1] de Munck, J.C., Wolters, C.H., Clerc, M.: In: Brette, R., Destexhe, A. (eds.) EEG and MEG: forward modeling, pp. 192–256. Cambridge University Press, Cambridge (2012). <https://doi.org/10.1017/CBO9780511979958.006>
- [2] Rullmann, M., Anwander, A., Dannhauer, M., Warfield, S.K., Duffy, F.H., Wolters, C.H.: EEG source analysis of epileptiform activity using a 1 mm anisotropic hexahedra finite element head model. *NeuroImage* **44**(2), 399–410 (2009)
- [3] Braess, D.: *Finite Elements: Theory, Fast Solvers, and Applications in Solid Mechanics*. Cambridge University Press, Cambridge (2007). <https://doi.org/10.1017/CBO9780511618635>
- [4] Niedermeyer, E., da Silva, F.L.: *Electroencephalography: Basic Principles, Clinical Applications, and Related Fields*. Lippincott Williams & Wilkins, Philadelphia (2004)
- [5] Kaipio, J.P., Somersalo, E.: *Statistical and Computational Methods for Inverse Problems*. Springer, Berlin (2004)
- [6] Hallez, H., Vanrumste, B., Grech, R., Muscat, J., De Clercq, W., Vergult, A., D’Asseler, Y., Camilleri, K.P., Fabri, S.G., Van Huffel, S., *et al.*: Review on solving the forward problem in eeg source analysis. *Journal of neuroengineering and rehabilitation* **4**(1), 46 (2007)
- [7] Pursiainen, S., Vorwerk, J., Wolters, C.H.: Electroencephalography (eeg) forward modeling via h(div) finite element sources with focal interpolation. *Physics in Medicine & Biology* **61**(24), 8502 (2016)
- [8] Medani, T., Lautru, D., Schwartz, D., Ren, Z., Sou, G.: FEM method for the EEG forward problem and improvement based on modification of the saint Venant’s method. *Progress In Electromagnetics Research* **153**, 11–22 (2015)
- [9] Seeber, M., Cantonas, L.-M., Hoevels, M., Sesia, T., Visser-Vandewalle, V., Michel, C.M.: Subcortical electrophysiological activity is detectable with high-density eeg source imaging. *Nature communications* **10**(1), 753

- (2019)
- [10] Cuffin, B.N., Schomer, D.L., Ives, J.R., Blume, H.: Experimental tests of EEG source localization accuracy in realistically shaped head models. *Clinical neurophysiology* **112**(12), 2288–2292 (2001)
- [11] Rezaei, A., Koulouri, A., Pursiainen, S.: Randomized Multiresolution Scanning in Focal and Fast E/MEG Sensing of Brain Activity with a Variable Depth. *Brain Topography* **33**(2), 161–175 (2020). <https://doi.org/10.1007/s10548-020-00755-8>
- [12] Hang, S.: TetGen, a Delaunay-based quality tetrahedral mesh generator. *ACM Trans. Math. Softw* **41**(2), 11 (2015)
- [13] Schöberl, J.: NETGEN, An advancing front 2D/3D-mesh generator based on abstract rules. *Computing and visualization in science* **1**(1), 41–52 (1997)
- [14] Geuzaine, C., Remacle, J.-F.: Gmsh: A 3-d finite element mesh generator with built-in pre-and post-processing facilities. *International journal for numerical methods in engineering* **79**(11), 1309–1331 (2009)
- [15] Dannhauer, M., Lanfer, B., Wolters, C.H., Knösche, T.R.: Modeling of the human skull in eeg source analysis. *Human brain mapping* **32**(9), 1383–1399 (2011)
- [16] Antonakakis, M., Schrader, S., Wollbrink, A., Oostenveld, R., Rampp, S., Haueisen, J., Wolters, C.H.: The effect of stimulation type, head modeling, and combined EEG and MEG on the source reconstruction of the somatosensory P20/N20 component. *Human brain mapping* **40**(17), 5011–5028 (2019)
- [17] Fang, Q., Boas, D.A.: Tetrahedral mesh generation from volumetric binary and grayscale images. In: 2009 IEEE International Symposium on Biomedical Imaging: from Nano to Macro, pp. 1142–1145 (2009). Ieee
- [18] Piastra, M.C., Nüfing, A., Vorwerk, J., Clerc, M., Engwer, C., Wolters, C.H.: A comprehensive study on electroencephalography and magnetoencephalography sensitivity to cortical and subcortical sources. *Human Brain Mapping* **42**(4), 978–992 (2021)
- [19] Athinoula A. Martinos Center for Biomedical Imaging: FreeSurfer (1999–2019)
- [20] Lo, D.S.H.: Finite Element Mesh Generation. Taylor & Francis, UK (2015). <https://books.google.fi/books?id=ZhEeBQAAQBAJ>
- [21] Dannhauer, M., Lämmel, E., Wolters, C.H., Knösche, T.R.: Spatio-temporal regularization in linear distributed source reconstruction from eeg/meg - a critical evaluation. *NeuroImage* (2012). submitted for publication
- [22] Piastra, M.C., Schrader, S., Nüfing, A., Antonakakis, M., Medani, T., Wollbrink, A., Engwer, C., Wolters, C.H.: The WWU DUNEuro reference data set for combined EEG/MEG source analysis. Zenodo (2020). <https://doi.org/10.5281/zenodo.3888381>
- [23] Michel, C.M., Brunet, D.: Eeg source imaging: a practical review of the analysis steps. *Frontiers in neurology* **10**, 325 (2019)
- [24] Hämäläinen, M.S., Ilmoniemi, R.J.: Interpreting magnetic fields of the brain: minimum norm estimates. *Med. & Biol. Eng. & Comp.* **32**, 35–42 (1994)
- [25] Pascual-Marqui, R.D.: Standardized low-resolution brain electromagnetic tomography (sloreta): technical details. *Methods and findings in experimental and clinical pharmacology* **24**, 5–12 (2002)
- [26] Fuchs, M., Wagner, M., Wischmann, H.-A., Köhler, T., Theißen, A., Drenckhahn, R., Buchner, H.: Improving source reconstructions by combining bioelectric and biomagnetic data. *Clinical Neurophysiology* **107**(2), 93–111 (1998)
- [27] Rezaei, A., Lahtinen, J., Neugebauer, F., Antonakakis, M., Piastra, M.C., Koulouri, A., Wolters, C.H., Pursiainen, S.: Reconstructing subcortical and cortical somatosensory

activity via the RAMUS inverse source analysis technique using median nerve SEP data. *NeuroImage* **245**, 118726 (2021)

- [28] Murphy, K.P.: *Machine Learning: A Probabilistic Perspective*. Adaptive Computation and Machine Learning. MIT press (2012)
- [29] He, Q., Rezaei, A., Pursiainen, S.: Zeffiro user interface for electromagnetic brain imaging: A gpu accelerated fem tool for forward and inverse computations in matlab. *Neuroinformatics* **18**(2), 237–250 (2020)
- [30] Miinalainen, T., Rezaei, A., Us, D., Nüßing, A., Engwer, C., Wolters, C.H., Pursiainen, S.: A realistic, accurate and fast source modeling approach for the eeg forward problem. *NeuroImage* **184**, 56–67 (2019)
- [31] Pellerin, J., Verhetsel, K., Remacle, J.-F.: There are 174 subdivisions of the hexahedron into tetrahedra. *ACM Transactions on Graphics (TOG)* **37**(6), 1–9 (2018)
- [32] Pursiainen, S.: Raviart–thomas-type sources adapted to applied eeg and meg: implementation and results. *Inverse Problems* **28**(6), 065013 (2012)
- [33] Delaunay, B., *et al.*: Sur la sphere vide. *Izv. Akad. Nauk SSSR, Otdelenie Matematicheskii i Estestvennyka Nauk* **7**(793-800), 1–2 (1934)
- [34] Hämäläinen, M.S., Hari, R., R. Ilmoniemi, Knuutila, J., O.Lounasmaa: Magnetoencephalography: theory, instrumentation, and applications to noninvasive studies of the working human brain. *Rev.Mod.Phys.* **65**, 413–497 (1993)
- [35] Bauer, M., Pursiainen, S., Vorwerk, J., Köstler, H., Wolters, C.H.: Comparison Study for Whitney (Raviart-Thomas) Type Source Models in Finite Element Method Based EEG Forward Modeling. *IEEE Transactions on Biomedical Engineering* **62**(11), 2648–56 (2015)
- [36] Zhang, Z.: A fast method to compute surface potentials generated by dipoles within multi-layer anisotropic spheres. *Physics in medicine & biology* **40**(3), 335 (1995)
- [37] Becker, H., Albera, L., Comon, P., Haardt, M., Birot, G., Wendling, F., Gavaret, M., Bénar, C.G., Merlet, I.: Eeg extended source localization: tensor-based vs. conventional methods. *NeuroImage* **96**, 143–157 (2014)
- [38] Kantorovich, L.V.: On one effective method of solving certain classes of extremal problems. *Akad. Nauk USSR* **28**, 212–215 (1940)
- [39] Vaserstein, L.N.: Markov processes over denumerable products of spaces, describing large systems of automata. *Problems Inform. Transmission* **5**(3), 47–52 (1969)
- [40] Rubner, Y., Tomasi, C., Guibas, L.J.: A metric for distributions with applications to image databases. In: *Sixth International Conference on Computer Vision (IEEE Cat. No.98CH36271)*, pp. 59–66 (1998). <https://doi.org/10.1109/ICCV.1998.710701>
- [41] Mahalanobis, P.C.: On the generalized distance in statistics. (1936). National Institute of Science of India
- [42] Ary, J.P., Klein, S.A., Fender, D.H.: Location of sources of evoked scalp potentials: corrections for skull and scalp thicknesses. *IEEE Transactions on Biomedical Engineering* **28**(6), 447–452 (1981)
- [43] Pursiainen, S., Sorrentino, A., Campi, C., Piana, M.: Forward simulation and inverse dipole localization with the lowest order raviart–thomas elements for electroencephalography. *Inverse Problems* **27**(4), 045003 (2011)
- [44] Shahid, S.S., Bikson, M., Salman, H., Wen, P., Ahfock, T.: The value and cost of complexity in predictive modelling: role of tissue anisotropic conductivity and fibre tracts in neuromodulation. *Journal of neural engineering* **11**(3), 036002 (2014)
- [45] Purves, D., Augustine, G.J., Fitzpatrick, D.,

- Hall, W., LaMantia, A.-S., White, L.: Neuroscience. Oxford University Press Inc, New York (2019)
- [46] Noël, P., Ozaki, I., Desmedt, J.E.: Origin of N18 and P14 far-fields of median nerve somatosensory evoked potentials studied in patients with a brain-stem lesion. *Electroencephalography and clinical neurophysiology* **98**(2), 167–170 (1996)
- [47] Buchner, H., Adams, L., Müller, A., Ludwig, I., Knepper, A., Thron, A., Niemann, K., Scherg, M.: Somatotopy of human hand somatosensory cortex revealed by dipole source analysis of early somatosensory evoked potentials and 3D-NMR tomography. *Electroencephalography and Clinical Neurophysiology/Evoked Potentials Section* **96**(2), 121–134 (1995)
- [48] Mauguière, F., Desmedt, J., Courjon, J.: Neural generators of N18 and P14 far-field somatosensory evoked potentials studied in patients with lesion of thalamus or thalamocortical radiations. *Electroencephalography and clinical neurophysiology* **56**(4), 283–292 (1983)
- [49] Urasaki, E., Wada, S.-i., Kadoya, C., Yokota, A., Matsuoka, S., Shima, F.: Origin of scalp far-field N18 of SSEPs in response to median nerve stimulation. *Electroencephalography and Clinical Neurophysiology/Evoked Potentials Section* **77**(1), 39–51 (1990)
- [50] Passmore, S.R., Murphy, B., Lee, T.D.: The origin, and application of somatosensory evoked potentials as a neurophysiological technique to investigate neuroplasticity. *The Journal of the Canadian Chiropractic Association* **58**(2), 170 (2014)
- [51] Buchner, H., Fuchs, M., Wischmann, H.-A., Dössel, O., Ludwig, I., Knepper, A., Berg, P.: Source analysis of median nerve and finger stimulated somatosensory evoked potentials: multichannel simultaneous recording of electric and magnetic fields combined with 3D-MR tomography. *Brain topography* **6**(4), 299–310 (1994)
- [52] Allison, T., Wood, C.C., McCarthy, G., Spencer, D.D.: Cortical somatosensory evoked potentials. II. Effects of excision of somatosensory or motor cortex in humans and monkeys. *Journal of neurophysiology* **66**(1), 64–82 (1991)
- [53] Papadelis, C., Eickhoff, S.B., Zilles, K., Ioannides, A.A.: BA3b and BA1 activate in a serial fashion after median nerve stimulation: direct evidence from combining source analysis of evoked fields and cytoarchitectonic probabilistic maps. *Neuroimage* **54**(1), 60–73 (2011)
- [54] Stok, C.J.: The influence of model parameters on EEG/MEG single dipole source estimation. *IEEE Trans. Biomed. Eng.* **34**, 289–296 (1987)
- [55] Huang, Y., Datta, A., Bikson, M., Parra, L.C.: Roast: An open-source, fully-automated, realistic volumetric-approach-based simulator for tes. In: 2018 40th Annual International Conference of the IEEE Engineering in Medicine and Biology Society (EMBC), pp. 3072–3075 (2018). <https://doi.org/10.1109/EMBC.2018.8513086>
- [56] Fabri, A., Pion, S.: Cgal: The computational geometry algorithms library. In: Proceedings of the 17th ACM SIGSPATIAL International Conference on Advances in Geographic Information Systems, pp. 538–539 (2009)
- [57] Schrader, S., Westhoff, A., Piastra, M.C., Miinalainen, T., Pursiainen, S., Vorwerk, J., Brinck, H., Wolters, C.H., Engwer, C.: Duneuro—a software toolbox for forward modeling in bioelectromagnetism. *PloS one* **16**(6), 0252431 (2021)
- [58] Tadel, F., Baillet, S., Mosher, J.C., Pantazis, D., Leahy, R.M.: Brainstorm: a user-friendly application for MEG/EEG analysis. *Computational intelligence and neuroscience* **2011**, 8 (2011)